Critical Analyses of Data Differences between FNMOC and AFGWC Spawned SSM/I Datasets

ADRIAN A. RITCHIE JR.,* MATTHEW R. SMITH,* H. MICHAEL GOODMAN,+ RONALD L. SCHUDALLA,* DAWN K. CONWAY,* FRANK J. LAFONTAINE,* DON MOSS,# AND BRIAN MOTTA*

* *Hughes STX, Global Hydrology and Climate Center (GHCC), Huntsville, Alabama*
+ *NASA/Marshall Space Flight Center, GHCC, Huntsville, Alabama*
# *University of Alabama in Huntsville, GHCC, Huntsville, Alabama*

(Manuscript received 5 December 1995, in final form 24 October 1996)

ABSTRACT

Antenna temperatures and the corresponding geolocation data from the five sources of the Special Sensor Microwave/Imager data from the Defense Meteorological Satellite Program *F11* satellite have been characterized. Data from the Fleet Numerical Meteorology and Oceanography Center (FNMOC) have been compared with data from other sources to define and document the differences resulting from different processing systems. While all sources used similar methods to calculate antenna temperatures, different calibration averaging techniques and other processing methods yielded temperature differences. Analyses of the geolocation data identified perturbations in the FNMOC and National Environmental Satellite, Data and Information Service data. The effects of the temperature differences were examined by generating rain rates using the Goddard Scattering Algorithm. Differences in the geophysical precipitation products are directly attributable to antenna temperature differences.

1. Introduction

Passive microwave imager data from the Department of Defense's Defense Meteorological Satellite Program (DMSP) Special Sensor Microwave/Imager (SSM/I) instruments are widely used in algorithms to generate geophysical parameters. *Remote Sensing Reviews* (Barrett 1994) dedicated a complete issue to the First WetNet Precipitation Intercomparison Project (PIP-1) that compared global satellite precipitation algorithms with the source data being primarily SSM/I. Recently, Ferraro (1996) published an eight-year time series of rainfall, clouds, water vapor, snow cover, and sea ice derived from SSM/I observations. Other scientists have produced geophysical products from the data; for example, Wentz (1992a) routinely produces cloud liquid water, integrated water vapor, and wind speed over the ocean; Atlas et al. (1996) generated multiyear global surface wind velocities; Neale et al. (1990) developed a land surface-type classification scheme; and McFarland et al. (1990) derived land surface temperature.

SSM/I data are used operationally in the generation of geophysical products by many centralized processing centers, including the U.S. Navy's Fleet Numerical Meteorology and Oceanography Center (FNMOC), National Oceanic and Atmospheric Administration's (NOAA) National Environmental Satellite, Data and Information Service (NESDIS), NOAA/National Centers for Environmental Prediction, and the U.S. Air Force Global Weather Center (AFGWC). For the research community, SSM/I temperatures, geolocation information, and derived geophysical products are made available by government agencies, for example, NOAA, as well as a commercial firm, Remote Sensing Systems (RSS). For many years, the National Aeronautics and Space Administration's (NASA) WetNet project distributed NESDIS Level 1b (L1b) data and derived products to an international group of scientists (Dodge and Goodman 1994). Data from RSS have been distributed to many scientists and were used as input to the NASA Marshall Space Flight Center's (MSFC) generation of SSM/I data and products for the NOAA/NASA Pathfinder program (Asrar and Greenstone 1995). The SSM/I data are also available for algorithm development from NOAA's National Geophysical Data Center (NGDC) and NESDIS.

While systematic errors in the same processing system can be accounted for, the analyses and interpretation of long-term records of temperatures and derived geophysical products are more difficult if the records contain data from multiple sources or geophysical products generated from different antenna temperature sources. The purpose of this study is to characterize and compare data available to the scientific community from the dif-

Corresponding author address: Dr. Adrian Ritchie Jr., GHCC, Research Park West, 977 Explorer Blvd., Huntsville, AL 35806.
E-mail: adrian.ritchie@msfc.nasa.gov

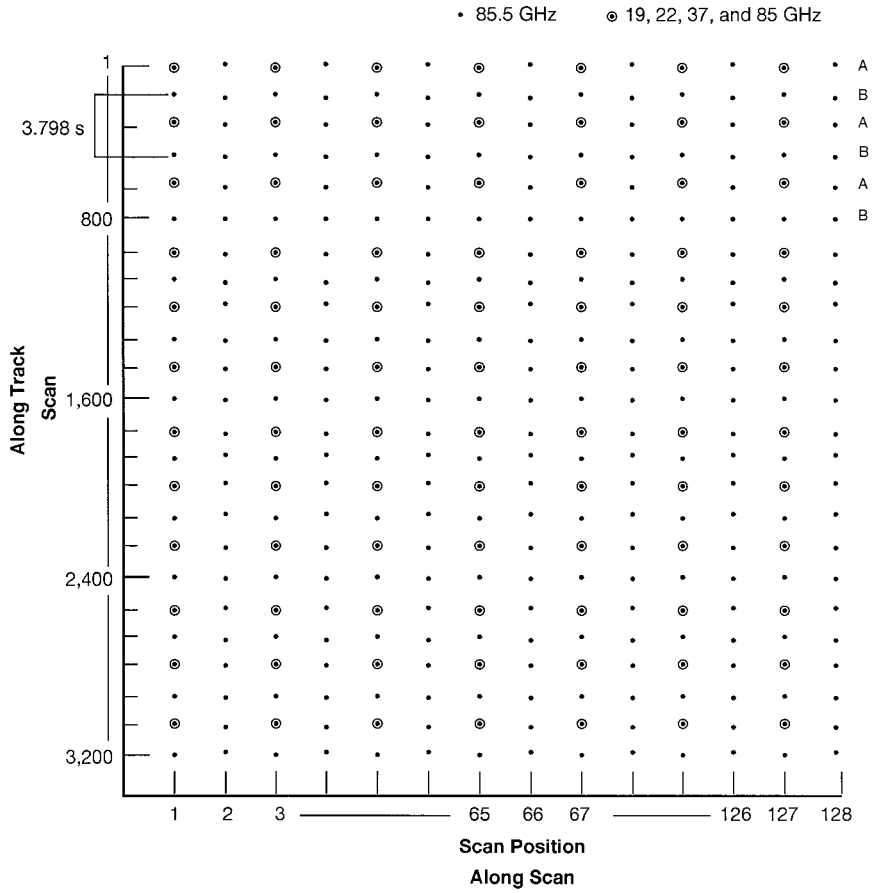

FIG. 1. SSM/I scan pattern. The low-resolution channels are dual polarized channels at 19.35 and 37.0 GHz plus the vertically polarized 22.235-GHz channel. These data are recorded at every other pixel on the A scan. The dual polarized 85.5-GHz channels are recorded at every pixel on both A and B scans.

ferent sources with mature processing systems, which will provide insight into the results of different processing methodologies and will serve as a foundation for improvements in the quality of the data made available to the research community.

Section 2 discusses the SSM/I data and gross characterization of the sources, including methods used to calculate antenna temperatures and differences in the scan start times. Examples from different orbits are used to show various aspects of the investigation. Sections 3 and 4 address the antenna temperature and geolocation comparisons, respectively. Section 5 compares rainfall estimates generated using the antenna temperatures from the sources, and section 6 summarizes the results.

2. Data description and source characterization

The SSM/I instrument measures passive microwave emissions in three dual polarized channels at 19.35, 37.0, and 85.5 GHz and a vertically polarized channel at 22.235 GHz, resulting in seven separate channels. Figure 1 shows the sampling scheme for each channel. The instrument spins at a constant rate of 31.6 revolutions min^{-1} or 1.90 s per scan (Hollinger et al. 1990). During each scan, the 85.5-GHz channels are sampled 128 times. The lower frequencies are sampled every other scan and 64 times in a scan. The scans containing all seven channels are referred to as A scans while the B scans contain only the 85.5-GHz channels. The data are downlinked in scan pairs (A and B scans), resulting in a constant 3.798 s between successive pairs. With an orbital period of approximately 102 min for the DMSP satellite, there are approximately 1610 scan pairs in an orbit. Antenna temperatures are generated by a linear equation involving scene counts and various calibration values. Thus, each orbit contains over 103 000 antenna temperatures for each low-frequency channel and over 412 000 observations for each 85.5-GHz channel. Approximately every orbit, the SSM/I data are simultaneously downlinked to FNMOC and AFGWC as part of the satellite's data stream. After processing, FNMOC sends the antenna temperature data [temperature data records (TDR)] to NESDIS for archival and distribution to the research community. This dataset will be hereafter

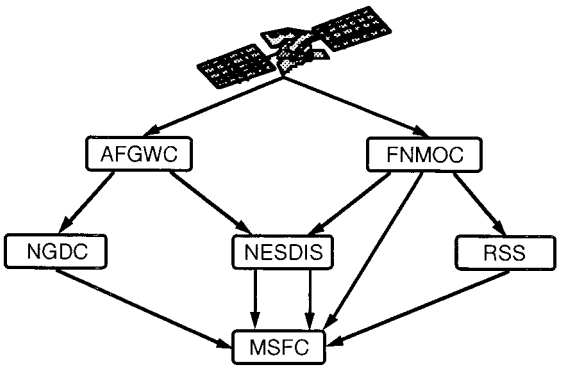

FIG. 2. Flow of SSM/I data from the DMSP satellite to MSFC.

identified as NESDIS TDR. RSS acquires the FNMOC antenna temperatures for use as the basis for the RSS antenna temperature dataset.

The other route the SSM/I data stream follows is through AFGWC. After some initial processing and archiving, data from all DMSP instruments are sent to NGDC. NGDC separates the instrument data streams and produces SSM/I antenna temperatures and geolocation information plus other instrument products. After additional internal processing at AFGWC, the AFGWC data are sent to NESDIS where antenna temperature and geolocation processing is performed. These data are referred to as NESDIS L1b. Figure 2 depicts the flow of SSM/I data used in the study.

Antenna temperatures and geolocation information from the DMSP F11 satellite for the period 1–7 April 1994 were obtained; this covers approximately 100 orbits. The sources were FNMOC, NGDC, RSS, and NESDIS, which provided two datasets, TDR and L1b. The data were organized into individual orbits, with the first scan occurring immediately after the satellite ascends over the equator. Because the instrument spin rate is constant, the time associated with each scan was used to coregister data from each source.

Figure 3 shows the number of scan pairs from each source for those orbits with greater than 1450 scan pairs. Because data were collected at different times and different places in the FNMOC and AFGWC processing systems, not all data were available for all orbits; 20% of all orbits from all sources had less than 1450 scan pairs. There is no pattern of missing orbits over the 100 orbits. Except for orbits 12075 and 12103, at least 60 scan pairs are missing for each orbit from each source. Most orbits have between 1500 and 1550 scan pairs out of approximately 1610 scan pairs, equating to 4–7 min of missing data. Visual inspection shows the majority of missing data occurred around the time of data transmission from the satellite to the ground receiving stations, and this is consistent with known data recorder problems on the satellite. A comparison of the NESDIS TDR and FNMOC data showed the data are identical except for 2–4 scan pairs per orbit that are unreadable in the NESDIS TDR data. This is attributed to a file formatting problem when NESDIS repackages the data into their archive format. In Fig. 3 the number of NESDIS TDR scan pairs is consistently less than the number of FNMOC scan pairs.

In this study, antenna temperatures outside the range of 50–325 K were classified as questionable and therefore may produce unreliable geophysical parameters. Nearly 25% of the FNMOC orbits have 1–10 question-

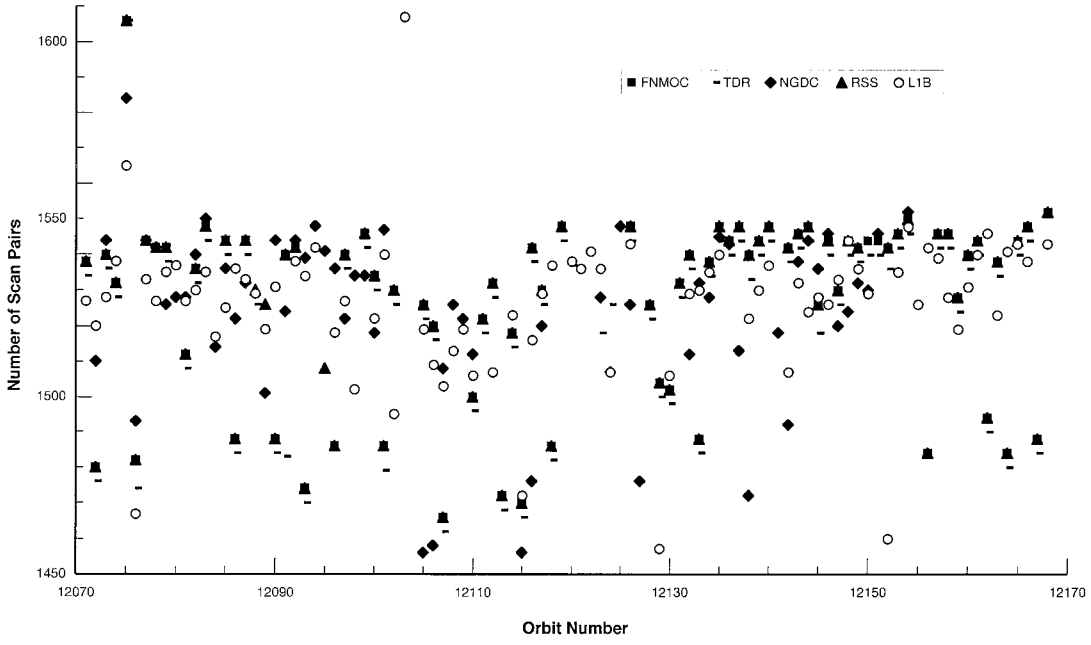

FIG. 3. Number of scans in each source for orbits with more than 1450 scan pairs.

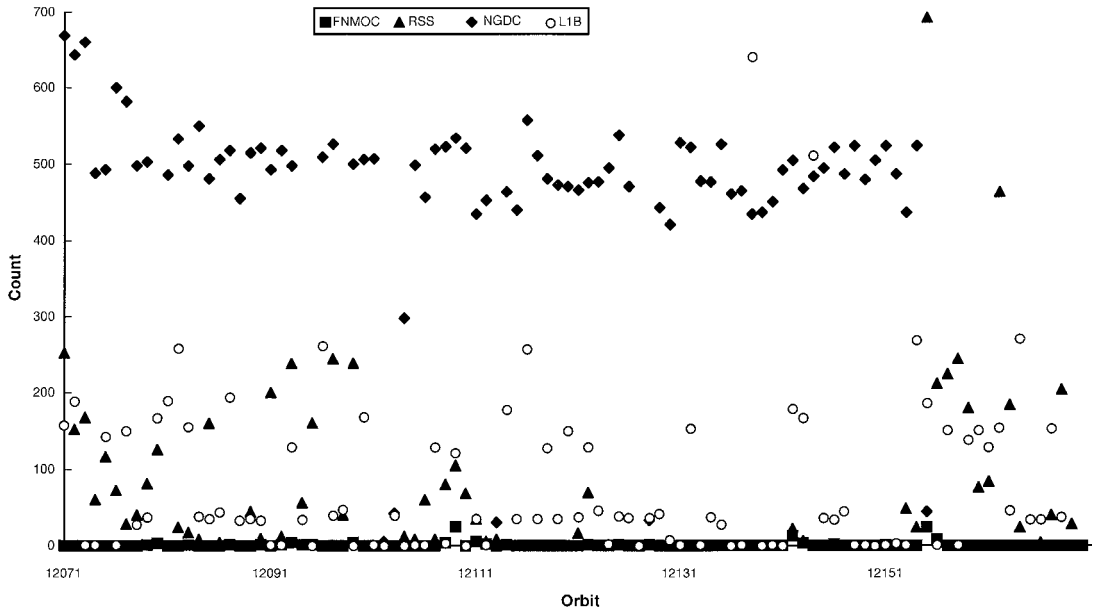

FIG. 4. Number of questionable antenna temperatures in each orbit by source.

able temperatures in at least one of the seven channels. The RSS data have a similar percentage of temperatures exceeding the thresholds except for the 85.5-GHz vertical channel. As part of the RSS quality control process, suspect temperatures are multiplied by -1 (Wentz 1992b), and these are classified as questionable in our evaluation. The NGDC and NESDIS L1b data have a larger number of questionable temperatures in all channels than is contained in the FNMOC data. The number of questionable temperatures in the 85.5-GHz vertical channel for all orbits and sources is plotted in Fig. 4. The NGDC data average 500–600 questionable temperatures per orbit, which is two orders of magnitude larger than the FNMOC data. The NESDIS L1b abnormal temperatures are more variable and average 100–200 per orbit. Although the number of questionable values may appear large, they are actually a small percentage of the total observations. For the 85.5-GHz channels, 500 values are less than 0.1% of the total number of samples in an orbit, which means 99.9% of the temperatures are acceptable.

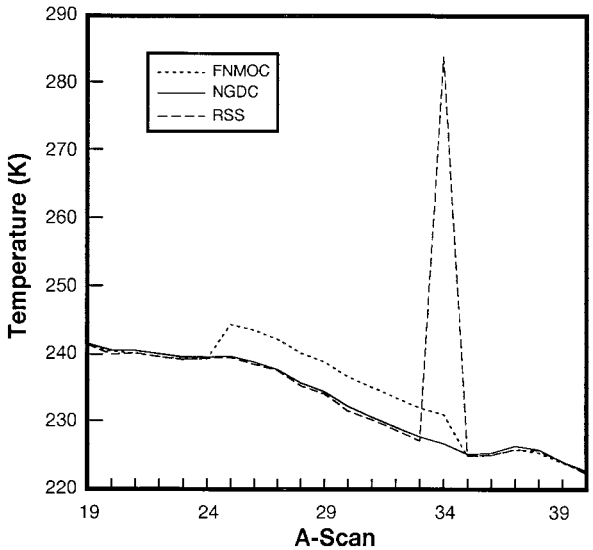

FIG. 5. 22.235-GHz vertical antenna temperatures by source for orbit 12143 at position 52. A scan 34 contains a bad calibration value. Since the data are processed in reverse time or scan order, erroneous calibration values in scan 34 affects scans 25–34.

Each source uses a different approach to obtain the calibration values used to generate antenna temperatures. As a result of the calibration/validation of the first instrument on the F8 DMSP satellite, FNMOC averages the calibration values over 10 scan pairs to reduce the noise. RSS calculates the antenna temperatures using only the calibration values associated with a particular scan. Since the input for the RSS process is the FNMOC antenna temperatures, the RSS system effectively reverses the FNMOC 10 scan pair averaging method, producing unsmoothed antenna temperatures (Wentz 1992b). NGDC also uses a 10 scan pair averaging process but removes the two highest and lowest values and averages the remaining six scan pairs. Figure 5 shows the effects of erroneous calibration values on the FNMOC 22.235-GHz vertical channel temperatures for a small subset of orbit 12143 at scan position 52. Erroneous calibration values in one scan cause over a 5 K increase in the temperatures for 10 scan pairs because of the averaging process. Since the data are processed in reverse time or scan order, the calibration error in scan 34 affects scans 25–34. Also plotted are the corresponding RSS data. In this case, since the RSS data

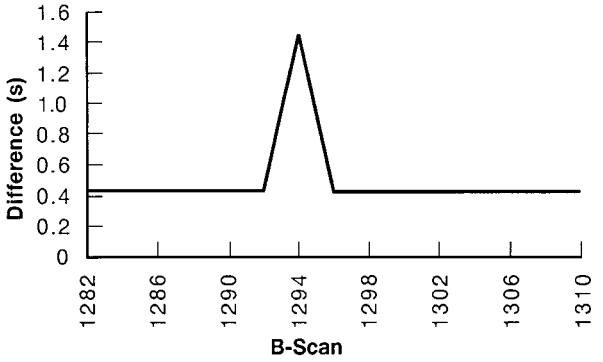

FIG. 6. B-scan start time differences in seconds between NGDC and FNMOC (NGDC − FNMOC) for orbit 12154.

are not averaged, the bad calibration affects only scan 34 and raises the temperature by nearly 60 K. The NGDC temperatures are also plotted, and by removing the high and low calibration values, the negative effects of averaging in bad calibration values are avoided.

Another area examined was the B-scan start times. The B scan, which contains only 85.5-GHz observations, is used as a reference scan for affixing the time of each scan pair. The FNMOC time information is not altered in the RSS and NESDIS TDR datasets, and thus, their B-scan start times are identical to the FNMOC times. The NGDC B-scan start times were offset from those of FNMOC by 0.42 s. This offset is applied by NGDC to more accurately geolocate the DMSP high-resolution visual and IR data. This offset is shown in Fig. 6, which plots start time differences (NGDC − FNMOC) for orbit 12154. It is also apparent in Fig. 6 that there are scan differences greater than or less than the expected 0.42 s. To determine the character of these anomalies, internal NGDC B-scan start time differences; that is, the time difference between successive B scans was also computed for orbit 12154. The plot in Fig. 7 shows the internal differences for the anomaly seen in Fig. 6. Since the difference between two successive B scans should be 3.79 s, the 4.75-s difference indicates a later-than-expected start time was assigned to scan 1294 during processing; scan 1295 is also later than expected. Scans before and after these two scans have times consistent with the 1.9 s rotation rate of the instrument.

The NGDC datasets are ''gap filled,'' meaning that all missing scan lines in the data are filled with flagged values. The number of scan lines inserted is a function of the time difference between the last good scan and the next good scan. In some orbits there are missing scans in the data, even though the data were purportedly gap filled. Further examination revealed that these missing scans occur at the beginning of an orbit file (when the spacecraft crosses the equator heading from south to north) and when there are data gaps between orbits.

The mean B-scan start time difference for the NESDIS L1b data is 3.79 s; however, the standard deviation

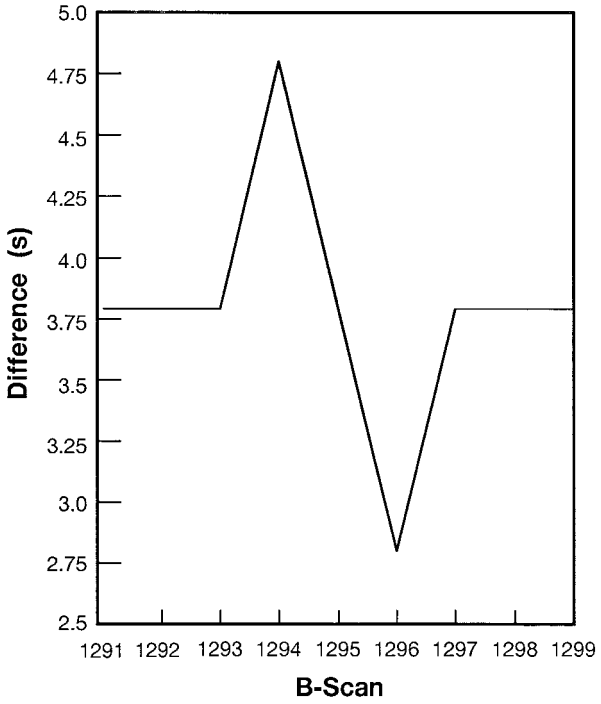

FIG. 7. NGDC B-scan start time internal differences for orbit 12154.

varied by orbit from 10^{-1} to 10^{-4} s. Figure 8 is a plot of the time differences between the NESDIS L1b and FNMOC scan start times for orbit 12103. The plot shows a ''sawtooth'' pattern with a period of approximately 100 scans with shorter wavelength oscillations superimposed. The internal B-scan start time deltas were cal-

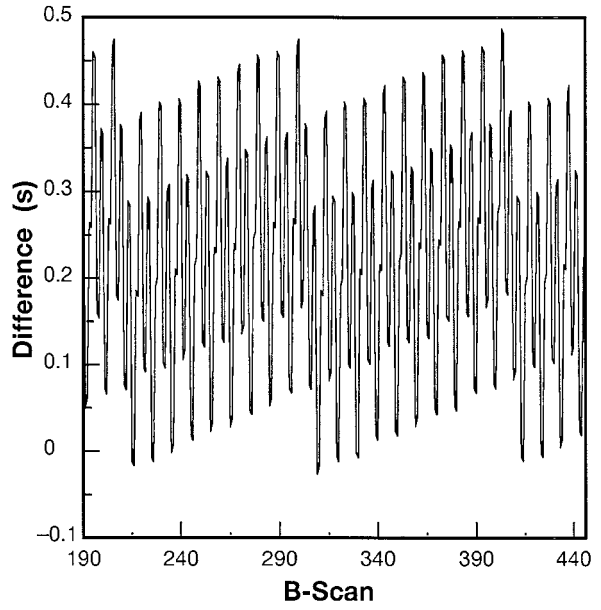

FIG. 8. B-scan start time differences between NESDIS L1b and FNMOC for orbit 12103.

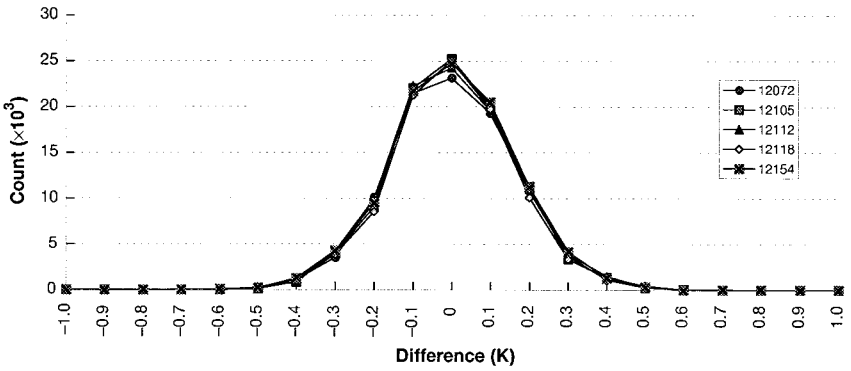

FIG. 9. Frequency plot of 19.35-GHz vertical antenna temperature differences between RSS and FNMOC for five orbits. Bins are 0.1 K wide, centered on 0.0.

culated for orbit 12103. The deltas range from 3.5 to 4.0 s and show a similar repetitive pattern.

3. Antenna temperature comparisons

The FNMOC antenna temperatures were designated as the baseline for the comparisons; temperatures from the other sources were compared with the FNMOC data. Missing and questionable values were not included in the comparison; that is, only pixels with valid antenna temperatures from both sources were included in the analyses. Various simple statistical parameters were generated for each orbit of each comparison. Except for the 2–4 unreadable scans in each orbit of the NESDIS TDR data (as explained in section 2), the FNMOC and NESDIS TDR datasets are identical. Therefore, no further analyses were performed between these two datasets.

RSS uses the FNMOC data as input to their process. The RSS output data are stored to the nearest 0.1 K while the FNMOC antenna temperatures are to the nearest 0.01 K. Based on rounding only, the differences should be nearly uniformly distributed. Since the RSS antenna temperatures are based on the individual scan calibration values while FNMOC averages 10 scans, the distribution of differences is nonuniform. The resulting difference distributions are shown in Fig. 9 for the 19.35-GHz vertical channel for five specific orbits. For orbit 12072, the differences are distributed around a mean of 0.0 K, with a standard deviation of 0.15 K. Results for all other orbits and channels are similar. The difference distributions and standard deviations are consistent throughout the 100 orbits with only slight orbit-to-orbit variations due to differences in the total number of pixels contained within each of the orbits. The differences in each 0.1-K frequency bin were also summed over all orbits, stratified by channel. The results are plotted in Fig. 10. The distributions of all channels are similar to the 19.35-GHz vertical channel shown in Fig. 9 in that the maximum number of differences are in the 0.0-K bin and the numbers rapidly decrease as size of the absolute value of the differences increases. The difference plots of the 22.235-GHz and 85.5-GHz vertical channels are much broader than the other. Only 58% and 60% of the differences in the 22.235-GHz and 85.5-GHz vertical channels, respectively, are within ± 0.15 K, while at least 68% of the data are in this range for the other channels.

The same methodology was used to compare the NGDC and FNMOC antenna temperatures. The differences in each channel were normalized by the total number of differences in the individual channels and plotted in Fig. 11. All channels show a distinct warm bias with the maximum number of differences usually occurring between 0.2 and 0.4 K. Approximately 98.8%–99.6% of the differences are less than ± 1.05 K, and these differences occur in all orbits.

The mean differences between the NESDIS L1b and FNMOC antenna temperatures are near 0.0 K with a standard deviation similar to the RSS results. For example, the NESDIS L1b standard deviation for the 37.0-GHz vertical channel of orbit 12072 is 0.1160 and the corresponding value for the RSS differences is 0.1189. The similarities between the NESDIS L1b − FNMOC and the RSS − FNMOC difference distributions are seen in Fig. 12 for the 19.35-GHz vertical and 37.0-GHz horizontal channels. Only 0.1%–0.2% of the differences are larger than ± 1.05 K, and for the low-resolution channels these differences do not occur in all orbits.

4. Geolocation comparisons

Geolocation data from the data sources were compared with those of FNMOC. The latitude and longitude values of each data source were not compared with each other directly, but the values were used to calculate distances or geolocation differences. In this way, directional variations were not compared. As mentioned in section 3, the FNMOC and NESDIS TDR datasets are nearly identical and thus there are no geolocation differences between NESDIS TDR and FNMOC datasets.

FNMOC generates geolocation values using the ephemeris information contained within the data stream

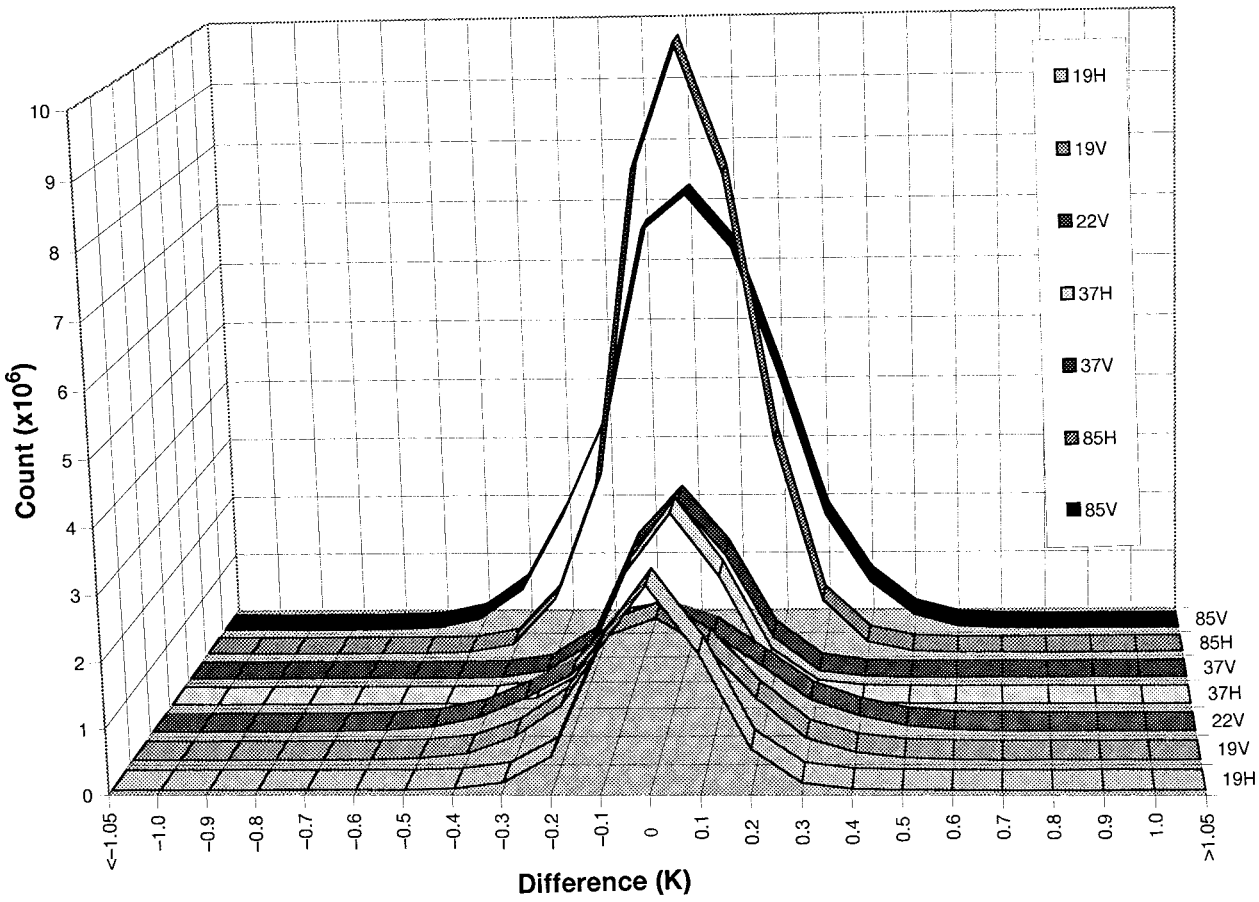

FIG. 10. Frequency plot of antenna temperature differences between RSS and FNMOC for all orbits by channel. Bins are 0.1 K wide, centered on 0.0.

and a scan geometry algorithm. During one of the source comparisons, a series of scans with large geolocation differences were detected. Close inspection of the FNMOC pixel latitude and longitude values revealed they did not always progress smoothly along and across

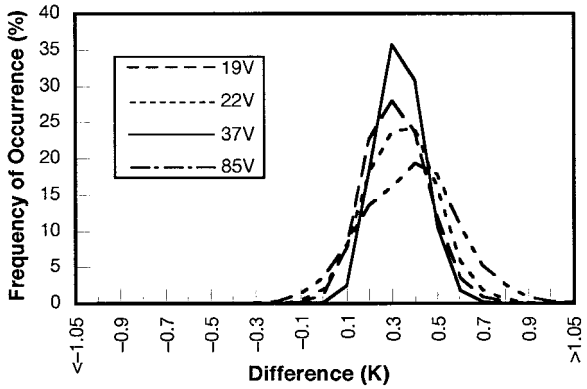

FIG. 11. Normalized frequency plot of antenna temperature differences between NGDC and FNMOC for four channels. The total count in each channel was used for normalization. Bins are 0.1 K wide, centered on 0.0.

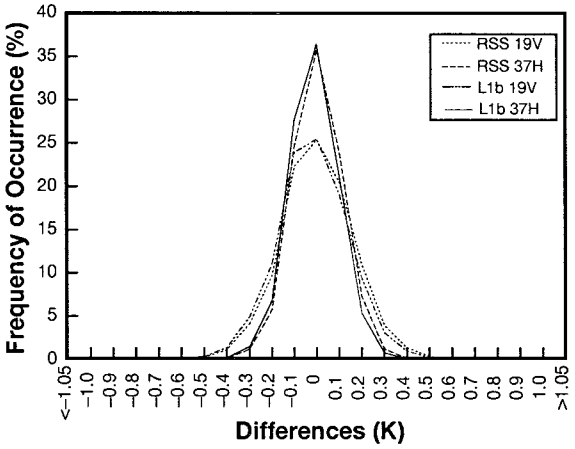

FIG. 12. Normalized frequency plot of antenna temperature differences between RSS and FNMOC, and NESDIS L1b and FNMOC for two channels. The total count in each channel was used for normalization. Bins are 0.1 K wide, centered on 0.0.

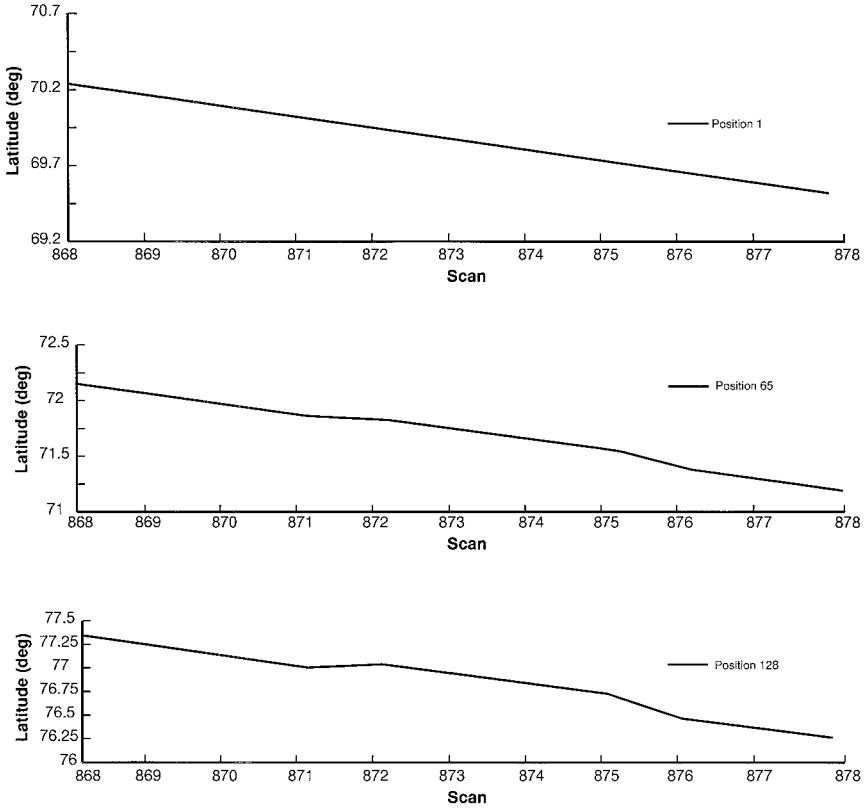

FIG. 13. FNMOC latitude values for orbit 12091 at three element positions.

the satellite track. Figure 13 is a plot of the longitudes for three pixel locations for a series of scans within orbit 12091. The perturbations or offsets are from 4 to 8 scans in length and have an amplitude as large as 0.4 deg. These offsets usually occur near the poles, are not limited to either side of a scan, and, in some instances, vary in amplitude along a scan. Seventy percent of the FNMOC orbits in this study contained at least one such offset of varying magnitude. Two orbits had three distinct offsets. However, the geolocation perturbations affect only 0.5% of the data.

Figures 14, 15, and 16 show along track and along scan geolocation differences for orbit 12072 between FNMOC and RSS, NGDC, and NESDIS L1b, respectively. Orbit 12072 is shown because it is representative of other orbits in this study. Distance differences for missing scans in either dataset have been set to zero. Table 1 summarizes the statistics of each source for this orbit.

RSS uses smoothed ephemeris and a satellite orbit model to generate latitude and longitude values. In order to reduce storage volume, RSS stores only 19 latitude and 19 longitude values per scan. However, RSS provides software to interpolate the remaining points. As seen in Fig. 14a, there is close overall agreement between the RSS and FNMOC geolocations for a pixel at the midpoint of the scan, with the mean differences for orbit 12072 being 1.5 km, with a standard deviation of 0.89 km. The spikes near scans 400 and 2400 resulted from perturbations in the FNMOC geolocations. In Fig. 14b, some of the 19 ''tie-down'' points are noticeable along the scan, but even the interpolated values are almost all less than 3 km.

NGDC uses the same satellite orbit model used by FNMOC. However, they use higher-precision data to navigate the satellite position because greater precision is needed for the higher-resolution visual and IR data. The distance differences are almost all less than 6 km, as seen in Fig. 15a. Since the satellite moves along track at 6.54 km s^{-1}, the 0.42-s offset in B-scan start time is responsible for up to 2.75 km of the geolocation differences. Figure 15b shows the along-scan differences for two scans (2175 and 2187) that are only 23 s apart. For scan 2175, the geolocation differences decrease from the start to the end of the scan, while for scan 2187 the differences increase from beginning to end. These inconsistent differences between scans are typical of the geolocation throughout the NGDC orbits.

NESDIS generates geolocations based on the ephemeris data provided by AFGWC and a pixel registration algorithm similar to FNMOC. Figure 16a shows differences as large as 20 km near the poles (centered on scans 800 and 2400). In Fig. 16b, there is a distinctive pattern to the along-scan difference variations. For this

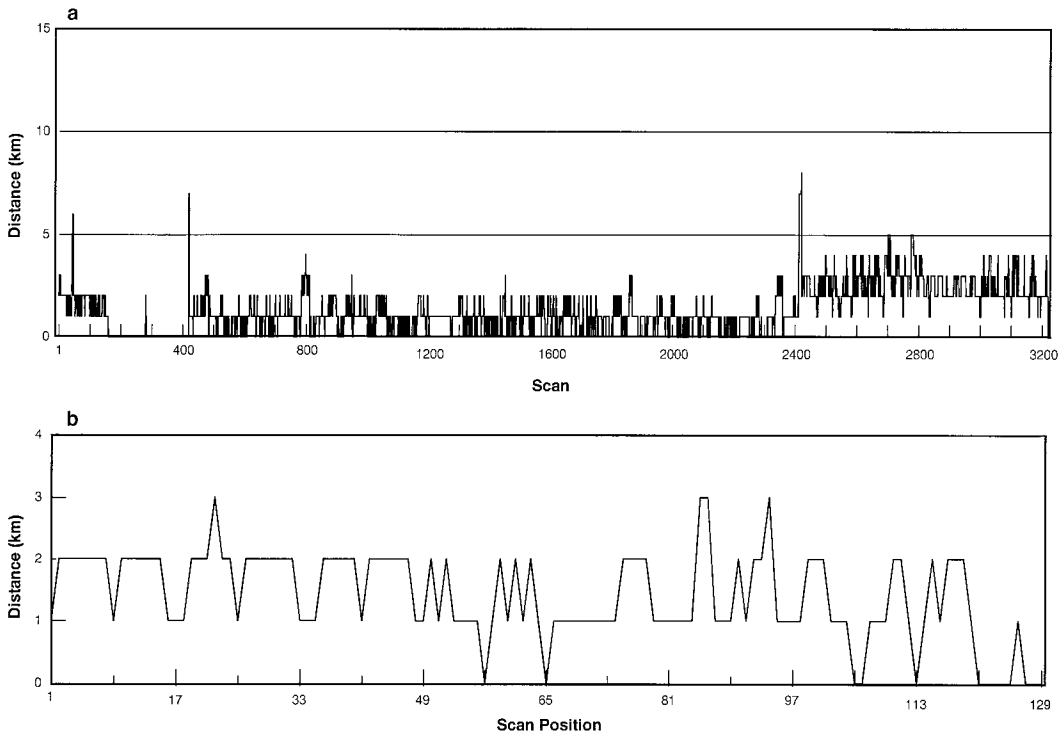

FIG. 14. Distance differences between RSS and FNMOC for orbit 12072: (a) Along-track differences at the midpoint of the scans (position 65), and (b) along-scan differences at scan 2177. The 19 pixel latitudes and longitudes contained in the dataset are at pixel locations 1, 9, 17, 25, 33, 41, 49, 57, 65, 73, 81, 89, 97, 105, 113, 121, 123, 127, and 128. Differences are rounded to the nearest kilometer.

orbit, differences were as large as 57 km at pixels not shown in the figures, and the mean of the difference is 7.5 km. Additionally, the latitudes and longitudes were quite noisy. Figure 17 shows an 80-scan portion (position 65, near the center of each scan) of latitudes as the satellite traversed the North Pole of orbit 12096. There is high-frequency noise superimposed on what should be a smoothly varying position trace. The variability of the B-scan start times plays a role in producing this noise.

5. Rain-rate algorithm comparison

After the antenna temperature differences were characterized, the objective was to determine the extent to which these differences affected the results of geophysical products. The Goddard Scattering Algorithm (GSCAT) (Adler et al. 1994), one of the global precipitation algorithms in the WetNet PIP-1 project, was selected. The algorithm is based on the results of the scattering of upwelling radiation by precipitation-size ice particles between the surface and intervening atmosphere at 85.5 GHz. The individual temperatures are subjected to a series of discriminators to filter observations that are likely not experiencing precipitation. At locations classified as raining, the rain rate is inversely proportional to the horizontally polarized antenna temperature at 85.5 GHz. The proportionality factor is a function of the underlying surface, such as land, water, or coast.

Since the mean temperature differences between RSS and FNMOC, and NESDIS L1b and FNMOC datasets were essentially zero, the rain rates were expected to be similar, and because of the warm bias in the NGDC data, the rain rates should be less. At pixels or locations classified as raining by GSCAT, each 0.1 K warm bias would decrease the rain rate by 0.024 mm h^{-1} over land and 0.048 mm h^{-1} over the ocean. The rain rates can also be affected by temperatures that are within the acceptable range but have been contaminated by bad calibration values or noise. Also, if the rain rates are binned into grids, geolocation differences can result in rain rates being improperly assigned, thereby affecting any statistics.

Three orbits (12072, 12082, and 12143) with only a few missing scans were used as input to the algorithm. Statistics were calculated for each dataset for two cases. In the first case, only pixels with valid rain rates in all datasets were included, while in the second case any pixel with a valid rain rate was included.

Table 2 shows results for the GSCAT for orbit 12082. Statistics for the other two orbits show similar patterns in the results. The number of raining A-scan pixels for each case are shown along with the mean rain rate. There

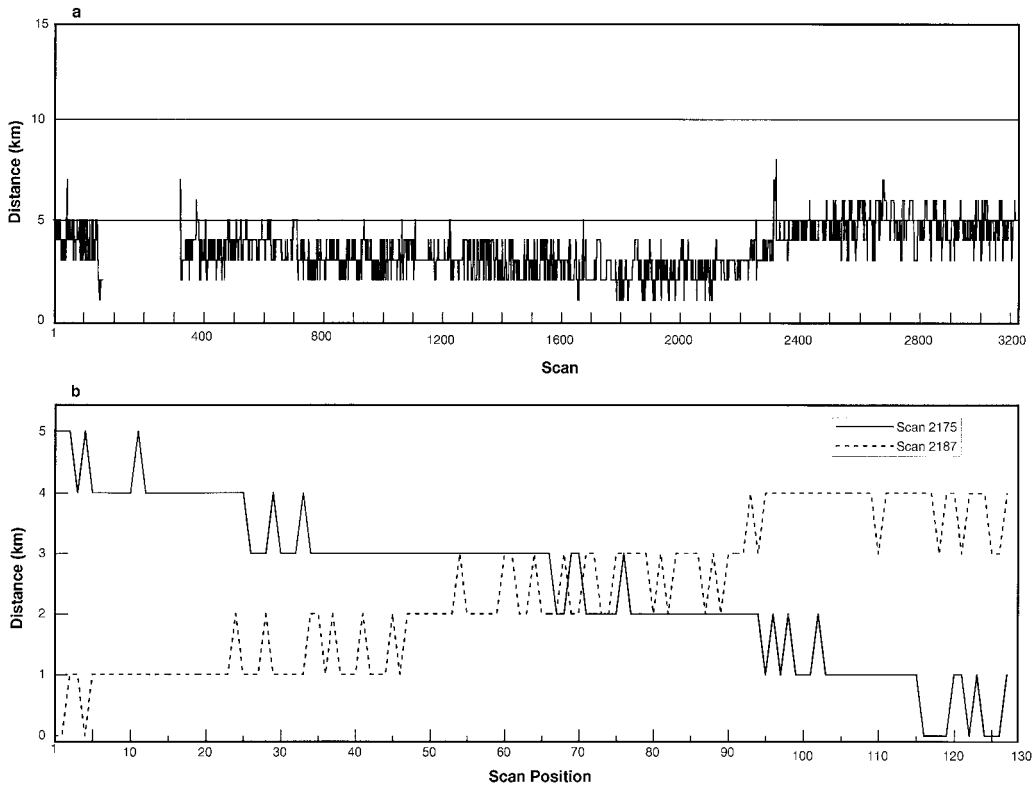

FIG. 15. Distance differences between NGDC and FNMOC for orbit 12072: (a) Along-track differences at the midpoint of the scans (position 65), and (b) along-scan differences at scans 2175 and 2187. Differences are rounded to the nearest kilometer.

are 1055 pixels classified as raining in all algorithms, with an additional 100 pixels classified as raining in at least one algorithm. For the orbits in this study, 1%–2% of the pixels are classified as raining. The bias is the difference between the mean data source rain rate and the mean FNMOC rain rate normalized by the algorithm rain rate. The ''total rain'' column is simply a sum of the rain rates (mm h^{-1}) at all pixels extrapolated for one hour. The mean rate and total rain for the FNMOC, NESDIS L1B, and RSS datasets are similar, with very small biases for both cases. The bias for the NGDC data is an order of magnitude larger for the first case and two orders of magnitude larger for the second case. Also, the sign of the NGDC bias changed between the cases. Since 98% of the horizontally polarized 85.5-GHz NGDC temperatures were warmer than the corresponding FNMOC temperatures, the smaller mean rate and smaller total rain for the NGDC dataset for the case where pixels in all sources were raining reflect the warm temperature bias. For the second case, which includes pixels characterized as raining in any source, the higher mean rate for the NGDC data result from temperatures that were within the acceptable range but differed from the FNMOC temperatures. Approximately 0.3% of the NGDC temperatures were greater than 1.05 K colder than the corresponding FNMOC temperatures with some of the differences as high as 103 K. These very cold temperatures can contribute large values to the rain rates, up to 89 mm h^{-1}. The cold NGDC temperatures in the additional 100 pixels in the case for rain in any algorithm resulted in the 3 mm h^{-1} increase in the mean rate for NGDC.

6. Summary

This macroscopic study demonstrates that there are differences among the various sources in both antenna temperatures and geolocation. While some specific causes have been suggested, it was not possible to determine all of them because the processing approaches of several sources were not available for study.

The FNMOC antenna temperatures contained few out-of-bound values. However, erroneous calibration data do contaminate antenna temperatures in 10 scan pairs because of the averaging process. Wentz (1993) estimates about 0.05% of the FNMOC scans contain erroneous calibration values. Also, at least one geolocation perturbation was detected in 70% of the FNMOC orbits.

The RSS processing approach is well documented (Wentz 1992b, 1993). Various techniques are used to modify the antenna temperatures based on calibration data from a single scan and to identify data that fail quality control. The latitudes and longitudes of the tem-

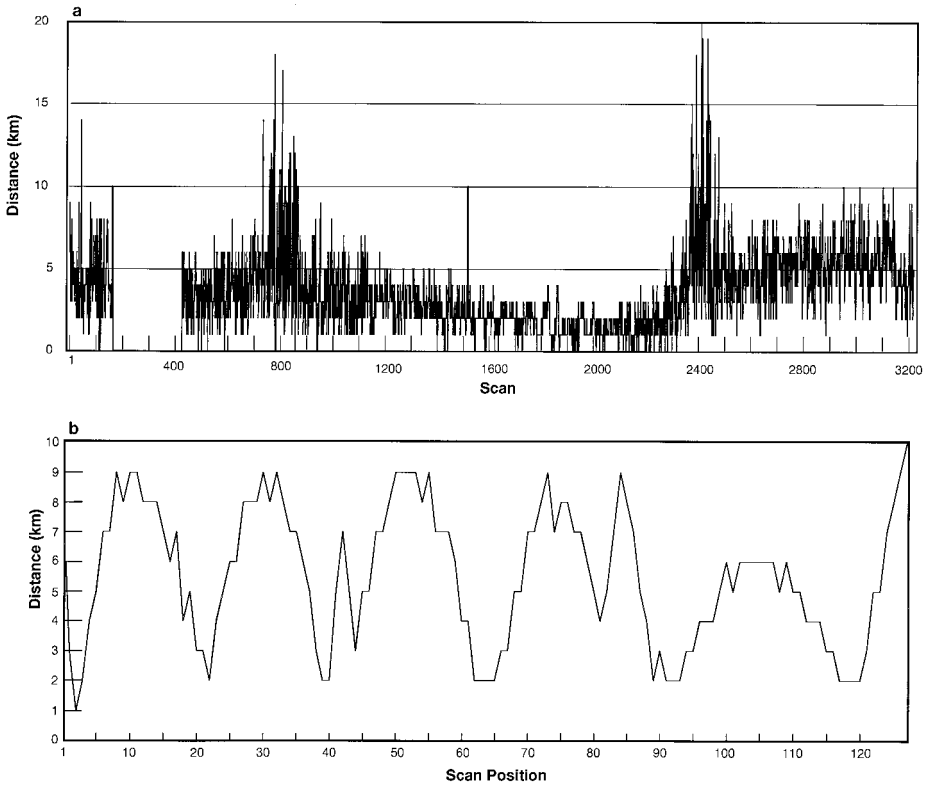

FIG. 16. Distance differences between NESDIS L1b and FNMOC for orbit 12072: (a) Along-track differences at the midpoint of the scans (position 65), and (b) along-scan differences at scan 117. Differences are rounded to the nearest kilometer.

perature data were determined from smoothed ephemeris data and were stored for every eighth scan position plus scan positions 123, 127, and 128. The mean distance difference between the FNMOC and RSS data is about 1.5 km with the distance differences at the 19 stored locations being smaller than those at the other 109 locations in a scan.

The temperature data from NGDC are generally 0.2–0.4 K warmer than the FNMOC data and contained a larger number of questionable values. The archiving system used by AFGWC in April 1994 has been replaced and is providing cleaner data. The number of questionable values should be lower, although the cleaner dataset has not been examined. The average distance difference between the NGDC and FNMOC data is near 3.5 km; the majority of this difference is attributed to the 0.42 s timing differential included in the NGDC processing.

The NESDIS L1b antenna temperatures contain more questionable values than FNMOC data, but in an aggregate sense, they are similar to the RSS temperatures. The distance differences increase rapidly near the poles,

TABLE 1. Summary of B-scan internal time differences for orbit 12072 for the four sources. The distance differences from FNMOC are included.

	B-scan start time internal differences (s)		Distance differences (km)		
Source	Mean	Std. dev.	Max	Mean	Std. dev.
FNMOC	3.7979	0.0002			
RSS	3.7979	0.0002	9	1.49	0.89
NGDC	3.7979	0.0271	10	3.43	1.265
NESDIS L1b	3.7982	0.1935	57	7.51	4.999

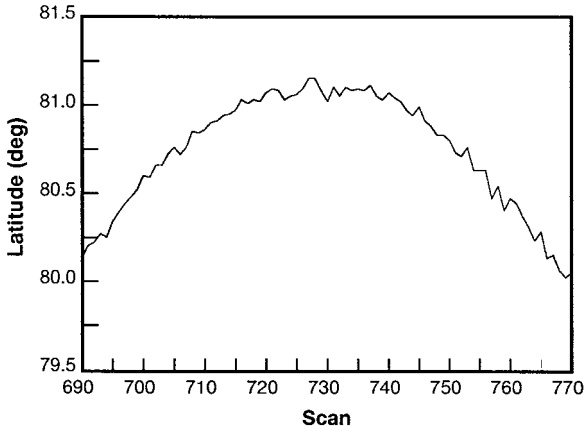

FIG. 17. NESDIS L1b latitude values for orbit 12096 at the midpoint of the scans (position 65).

TABLE 2. Results of the GSCAT for orbit 12082. The number of pixels classified as raining in all four sources is 1055. The number of pixels classified as raining in any source is 1155.

	Pixels with rain in all sources			Pixels with rain in any source		
Source	Mean rate	Bias (%)	Total rain (mm)	Mean rate	Bias (%)	Total rain (mm)
FNMOC	8.31		8768	7.64		8826
RSS	8.3	−0.1	8761	7.63	−0.1	8814
NGDC	8.22	−1.1	8674	10.62	38.9	12 260
NESDIS L1b	8.33	0.2	8785	7.66	0.2	8842

with some differences exceeding 50 km. There are also numerous high-frequency perturbations contained in all the geolocations, probably caused in part by the irregular scan start times.

Differences in the GSCAT rain rates mirror the antenna temperatures differences. Since the mean temperature difference for the RSS and FNMOC, and NESDIS L1b and FNMOC, are nearly zero, the rain rates are similar. The warm bias in the NGDC data leads to lower rain rates. Large numbers of temperature differences exceeding 1.05 K can yield a larger or smaller rain rate, depending on the sign of the difference. Since approximately 0.2% of the NGDC temperatures are colder than the FNMOC temperatures, it is possible to have larger rain rates generated from the NGDC data.

The antenna temperature processing methodology is the first of many steps in the process to generate specific geophysical products. These include an along-scan adjustment that Wentz (1992b) recommends, the cross-calibration of various instruments, and the antenna pattern correction used to compute brightness temperatures. The quantification of the sensitivity of different geophysical parameters to changes in the processing from scene counts to brightness temperatures would be a fruitful area of investigation. This is important because changes due to climate change may be masked by changes due to different processing approaches.

Acknowledgments. This study was performed as part of the NOAA/NASA Pathfinder project at the request of M. Maiden, the NASA Headquarters Pathfinder project manager. The authors thank each of the sources, FNMOC, RSS, NGDC, and NESDIS. Their cooperative attitude and help made it easy to acquire and process the data. We also thank T. Blanton of New Technology, Inc., for his help with the statistical analyses. We also thank the reviewers for their insightful suggestions and comments.

REFERENCES

Adler, R. F., G. J. Huffman, and P. R. Keehn, 1994: Global tropical rain estimates from microwave adjusted geosynchronous IR data. *Remote Sens. Rev.,* **11,** 125–152.

Asrar, G., and R. Greenstone, Eds., 1995: MTPE EOS reference handbook. EOS Project Office NP-215, 277 pp. [Available from EOS Project Office, NASA/Goddard Space Flight Center, Greenbelt, MD 20771.]

Atlas, R., R. N. Hoffman, S. C. Bloom, J. C. Jusem, and J. Ardizzone, 1996: A multiyear global wind velocity dataset using SSM/I wind observations. *Bull. Amer. Meteor. Soc.,* **77,** 869–882.

Barrett, E. C., Ed., 1994: The first WetNet Precipitation Intercomparison Project (PIP-1). *Remote Sens. Rev.,* **11,** 1–373.

Dodge, J. C., and H. M. Goodman, 1994: The WetNet Project. *Remote Sens. Rev.,* **11,** 5–23.

Ferraro, R. R., F. Weng, N. C. Grody, and A. Basist, 1996: An eight-year (1987–1994) time series of rainfall, clouds, water vapor, snow cover, and sea ice derived from SSM/I measurements. *Bull. Amer. Meteor. Soc.,* **77,** 891–905.

Hollinger, J. P., J. L. Peirce, and G. A. Poe, 1990: SSM/I instrument evaluation. *IEEE Trans. Geosci. Remote Sens.,* **28,** 781–790.

McFarland, M. J., R. L. Miller, and C. M. U. Neale, 1990: Land surface temperatures derived from the SSM/I passive microwave brightness temperatures. *IEEE Trans. Geosci. Remote Sens.,* **28,** 839–845.

Neale, C. M. U., M. J. McFarland, and K. Chang, 1990: Land-surface type classification using microwave brightness temperatures from the Special Sensor Microwave Imager. *IEEE Trans. Geosci. Remote Sens.,* **28,** 829–838.

Wentz, F. J., 1992a: Measurement of oceanic wind vector using satellite microwave radiometers. *IEEE Trans. Geosci. Remote Sens.,* **30,** 960–972.

——, 1992b: Final report production of SSM/I data sets. Remote Sensing Systems Tech. Rep. 090192, 72 pp. [Available from Remote Sensing Systems, 1101 College Ave., Suite 220, Santa Rosa, CA 95404.]

——, 1993: User's manual SSM/I antenna temperature tapes, revision 2. Remote Sensing Systems Tech. Rep. 120193, 34 pp. [Available from Remote Sensing Systems, 1101 College Ave., Suite 220, Santa Rosa, CA 95404.]